INTERNATIONAL JOURNAL FOR NUMERICAL METHODS IN FLUIDS
Int. J. Numer. Meth. Fluids 2005; **49**:465–488
Published online 14 June 2005 in Wiley InterScience (www.interscience.wiley.com). DOI: 10.1002/fld.998

Study on flow past two spheres in tandem arrangement using a local mesh refinement virtual boundary method

Jian-Feng Zou*,†, An-Lu Ren‡ and Jian Deng

Department of Mechanics, Research Institute of Fluid Engineering, Zhejiang University, Hangzhou, 310027, People's Republic of China

SUMMARY

A local mesh refinement virtual boundary method based on a uniform grid is designed to study the transition between the flow patterns of two spheres in tandem arrangement for $Re = 250$. For a small gap ($L/D = 1.5$), the flow field is axisymmetric. As the spacing ratio increases to 2.0, the pressure gradient induces the circumferential fluid motion and a plane-symmetric flow is constructed through a regular bifurcation. For $L/D \geqslant 2.5$, the vortices are periodically shed from the right sphere, but the planar symmetry remains. The case for $L/D = 3.0$ is picked up to give a detail investigation for the unsteady flow. The shedding frequency of vortical structure from the upper side of the right sphere is found to be double of the frequency of the lower side. With the flow spectra of various gaps given, the underlying competitive mechanism between the two shedding frequencies is studied and a critical spacing gap is revealed. Copyright © 2005 John Wiley & Sons, Ltd.

KEY WORDS: flow past two spheres; local mesh refinement; virtual boundary method

1. INTRODUCTION

The flow past a sphere is a fundamental problem in fluid dynamics. Although a sphere is the simplest geometry, a lot of natural and engineering applications exist, such as air pollution, combustion system and chemical processes, etc. The physical behaviour of the flow past a single sphere has been studied experimentally by some researchers (see References [1–3]) and the transitions between different flow regimes were revealed, described as follows. The flow begins to separate from the surface to form a stable and axisymmetric toroidal vortex at $Re = 24$, where Re is defined in terms of the uniform flow velocity and the diameter of the

*Correspondence to: J.-F. Zou, Department of Mechanics, Research Institute of Fluid Engineering, Zhejiang University, Hangzhou, 310027, People's Republic of China.
†E-mail: cnjianfengzou@hotmail.com
‡E-mail: renanlu@zju.edu.cn

Contract/grant sponsor: National Natural Science Foundation; contract/grant number: 10272094

Received 28 January 2005
Revised 14 April 2005
Accepted 23 April 2005

sphere. As the Reynolds number increases, the flow changes to an asymmetric but stable flow through a kind of regular bifurcation at $Re = 210$ and the flow field is characterized with the so-called double-threads wake. An unstable oscillating flow is achieved at $Re > 270$ and the hairpin-shaped vortices are periodically shed from the rear of the sphere.

Since 1990s, a number of numerical simulations for flow past a single sphere have been performed. But being restricted by the speed of CPU, the storage capacity and the mathematic algorithm, the assumption of axisymmetric flow that is incorrect for $Re > 210$ had to be made in the most simulations. Only recently, the primitive 3D unsteady Navier–Stokes equations were solved by Johnson and Patel [4] and Sungsu [5] to simulate the flow of a single sphere and their results compare well with previous experimental observations.

A little experimental work has been carried out for the investigation of the interaction of the wakes of two spheres in various arrangements. In early 1980s, some qualitative experimental results for flow past two or three spheres were achieved by Tsuji *et al.* [6]. The latest experimental study about wakes of two spheres placed side-by-side was done by Schouveiler *et al.* [7] and distinctly different regimes of interactions were observed, depending on the gap between two spheres.

In our knowledge, due to the difficulty in grid generation for the multiple-connected domain, no numerical method based on finite difference has been reported to successfully simulate the full flow past two or more spheres. To avoid this obstacle, for flow past two spheres placed side-by-side at low Reynolds numbers, a certain symmetry was assumed and the computational domain was reduced to only one quarter of an ellipsoid-like field by Kim and Elghobashi [8]. Thus, the calculation was performed on a simple-connected domain containing only one quarter of a single sphere and the dependence of the force on the distance between the two spheres and the vortex structure in the gap were investigated.

In our study, the virtual boundary method first presented by Goldstein *et al.* [9] was extended to a 3D application; then the 3D version was improved to handle local grid refinement by the implementation of a modified multigrid method. In our computations, the solution is predicted to vary rapidly in the boundary layers and a sufficiently fine grid system is required to precisely solve the flow in such region. Some test cases of our computations proved that a huge number of meshes have to be solved for a good resolution of boundary layer, which is not a feasible simulation for current computer capacity. A nonuniform grid is a suggested remedy. But in the context of finite difference technique, uneven grid size leads to more complex computer codes and more expensive costs which departs from the original spirit of the virtual boundary method on uniform Cartesian grid. Indeed, the local refinement virtual boundary method will give a good resolution in the boundary layers without losing the high performance. The currently modified virtual boundary method is used to study the interaction between the upstream and the downstream wake.

2. NUMERICAL METHOD

2.1. Virtual boundary method

The so-called virtual boundary method based on a uniform grid was first presented by Goldstein to model a no-slip boundary in flow field. The solid domain is assumed to be filled with fluid and a virtual force field is introduced into the Navier–Stokes equations, such that

a desired velocity distribution can be assigned to the fluid points on no-slip boundary. The virtual force field introduced in his work is governed by the following feed-back loop:

$$\mathbf{F}(\mathbf{x}_s, t) = \alpha \int_0^t [\mathbf{u}(\mathbf{x}_s, \tau) - \mathbf{v}(\mathbf{x}_s, \tau)]\, d\tau + \beta[\mathbf{u}(\mathbf{x}_s, t) - \mathbf{v}(\mathbf{x}_s, t)] \tag{1}$$

where α and β are two negative constants, $\mathbf{x}_s$ denotes a boundary point and $\mathbf{u}(\mathbf{x}_s, t)$ is the fluid velocity at $\mathbf{x}_s$; the velocity of the solid boundary point itself is $\mathbf{v}(\mathbf{x}_s, t)$. By using a pseudo-spectral method, Goldstein applied this procedure to simulate a start up flow around a stationary cylinder. To precisely define the no-slip boundary condition, large enough $|\alpha|$ and $|\beta|$ are needed, which unfortunately makes the governing equations stiff and the stability limit rigid. A Courant–Friedrichs–Lewy (CFL) number with an order of 10^{-3} is used in Goldstein's simulation. The expensive time cost makes the simulation of flow in complex geometry impossible. Therefore, an alterative expression for the virtual force of a no-slip boundary was provided by Fadlun *et al.* [10]

$$\mathbf{F}^{n+1} = -\mathbf{RHS}^n + \frac{\mathbf{v}^{n+1} - \mathbf{u}^n}{\Delta t} \tag{2}$$

where $\mathbf{v}^{n+1}$ is the velocity of solid boundary point at the next time level $t + \Delta t$, and $\mathbf{u}^n$ is the corresponding fluid velocity at t time level; the term $\mathbf{RHS}^n$ contains the convective, viscous and pressure gradient terms in momentum equation at t time level. Thus, at every time level the boundary condition can be defined exactly and no rigid stability limit is resulted in with the virtual force Equation (2) introduced into the Navier–Stokes equations.

In order to represent the boundary in the flow problem with complex geometry, Goldstein got a step-surface resulting from applying the body force only to the grid sites near the boundary and the values of physical properties needed to compute virtual force can be obtained directly from the flow field. In Fadlun's code, the velocity at the first grid point outside the body is obtained by linearly interpolating the velocity at the second point and the velocity at the body surface. Then the virtual force is computed for the first grid point in the flow field with the interpolated values.

In our computation, the boundary is defined following the approach provided by Saiki and Biringen [11]. We represent the sphere surface in a manner independent of the grid sites. The schematic distribution of virtual points on surface is shown in Figure 1 (actually there are more than 86 000 virtual points on the sphere). Thus, a kind of interpolation procedure would be needed to exchange the information between the virtual points and the adjacent grid points. Here, the fluid velocity at a virtual point is interpolated from the 8 adjacent grid points using a trilinear scheme in three dimensions

$$\mathbf{u}(\mathbf{x}_s) = \sum_{m=1}^{8} N_m(\mathbf{x}_s)\mathbf{u}_m \tag{3}$$

where the numbering of the velocities on grid points and the weights is given in Figure 2. In Figure 2, (ξ, η, ζ) denote the local transformational coordinates. The expression of the weight values in 8 grid points can be written as

$$N_m = \tfrac{1}{8}(1 + \xi_m\xi)(1 + \eta_m\eta)(1 + \zeta_m\zeta) \tag{4}$$

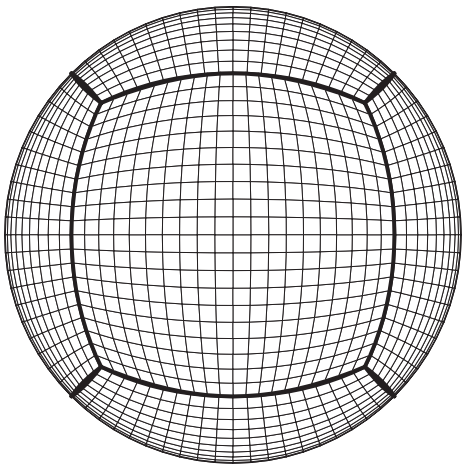

Figure 1. Distribution of virtual points.

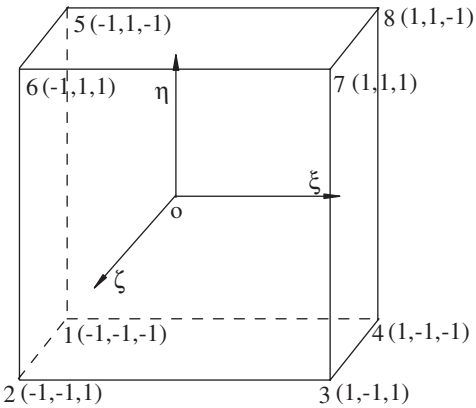

Figure 2. Numbering of interpolation points.

The virtual force at a virtual point is obtained using the feed-back expression given in Equation (1). Then the effect of the virtual force acting on the virtual point is spread back to the adjacent grid points by volume-weighted extrapolation

$$\mathbf{F}_m = \frac{1}{N_\mathrm{b}} \sum_{n=1}^{N_\mathrm{b}} N_m(\mathbf{x}_s)\mathbf{F}_n(\mathbf{x}_s) \tag{5}$$

where N_b is the number of the virtual points that affect the grid point. It should be noted that the virtual force on body surface is obtained using Goldstein's feed-back expression rather than Fadlun's momentum force. The expression of Fadlun's momentum force contains the first and second order derivatives of physical properties and a few more grid points are needed for the construction of finite difference equations, which will influence the resolution in the boundary layer region.

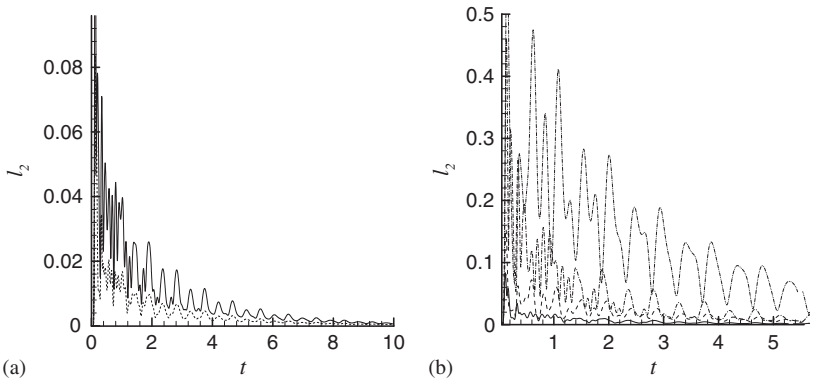

Figure 3. Time histories of l_2-norm error for the simulation of a single cylinder: (a) dashed line: case with internal virtual force; solid line: case without internal virtual force; (b) solid line: $\alpha = -40000$, $\beta = -600$; dashed line: $\alpha = -4000$, $\beta = -600$; dashdotted line: $\alpha = -4000$, $\beta = -60$; dashdotdotted line: $\alpha = -400$, $\beta = -60$.

In their computations, Goldstein and Fadlun imposed the virtual force only at the boundary; thus, unphysical fluid motion was allowed inside the body. In our test cases, if the virtual force was introduced only on the surface, no converged solution was achieved for large Reynolds number flow. For the remedy of this problem, we impose the momentum force, given in Equation (2), at the grid points inside the body directly; no interpolation or extrapolation is needed in this procedure. Due to the perfect behaviour of Fadlun's expression mentioned previously, the computational performance has come to a considerable improvement. Figure 3(a) gives the time histories of the l_2-norm error for two 2D cases, i.e. the flow past a single cylinder without and with internal virtual force. The l_2-norm error in the streamwise velocity is defined as

$$l_2\text{-norm} = \sqrt{\frac{1}{N_\mathrm{b}} \sum_{n=1}^{N_\mathrm{b}} \mathbf{u}_n(\mathbf{x}_\mathrm{s}) * \mathbf{u}_n(\mathbf{x}_\mathrm{s})} \tag{6}$$

In Figure 3(a), the solid line denotes the case with virtual force computed only on the boundary, the dashed line for the case with internal virtual force. It is clear that the latter case brings the fluid near boundary to rest more rapidly. Consider the time histories of the l_2-norm error under different combinations of α and β (see Figure 3(b)), $\alpha = -4000$ and $\beta = -60$ are applied in all the following computations which can define a sufficiently precise boundary and allow a reasonable CFL number as well. For all the results provided in Section 4, the Goldstein's approach is utilized to model the no-slip boundary and the Fadlun's momentum force expression is imposed at the grid point within the body.

2.2. *Solution of governing equations*

The non-dimensional Navier–Stokes equations for incompressible viscous flow are written as

$$\begin{aligned} \nabla \cdot \mathbf{V} &= 0 \\ \frac{D\mathbf{V}}{Dt} &= -\nabla p + \frac{1}{Re} \nabla^2 \mathbf{V} + \mathbf{F} \end{aligned} \tag{7}$$

where $\mathbf{F}=(F_x,F_y,F_z)$ is the virtual force vector. The diameter D is used as the length scale and the uniform free-stream velocity is the characteristic velocity.

A rectangular computational domain is designed. A free-stream velocity condition is used at the inflow and far-field boundaries. A nonreflecting condition is used at the outflow boundary. A pressure Neumann condition is applied to inflow, far field and outflow boundaries and there is no pressure condition needed for the no-slip boundary. The initial flow field is at rest.

The momentum equations are solved using a finite difference method with implicit treatment of the convection and diffusion terms. The pressure variable is solved from the pressure Poisson equation which is derived by applying the divergence operator to the momentum equations. The time-dependent term of the pressure Poisson equation is handled by Harlow's method [12]. To satisfy the compatibility condition, the pressure condition is evaluated at half-grid points near boundary [13, 14]. The spatial derivatives in governing equations are discretized by second-order central difference. The present computation was done using Cartesian grid, and a collocated arrangement of variables. But unlike the SIMPLE algorithm for collocated grid which apply momentum interpolation to avoid check-board phenomenon, the author achieved smooth solution by directly discretizing the pressure Poission equation using central second-order finite scheme. And a continuity correction was done by partially considering the contribution of the discrete pressure equation derived from the discrete momentum equations.

The finally obtained algebraic equations system can be formally written as

$$\begin{aligned}
&C_{\mathrm{W}}u_{i-1,j,k}+C_{\mathrm{E}}u_{i+1,j,k}+C_{\mathrm{S}}u_{i,j-1,k}+C_{\mathrm{N}}u_{i,j+1,k}+C_{\mathrm{B}}u_{i,j,k-1}+C_{\mathrm{T}}u_{i,j,k+1}+C_{\mathrm{C}}u_{i,j,k}\\
&\quad=\frac{u^0_{i,j,k}}{\Delta t}-\frac{p_{i+1,j,k}-p_{i-1,j,k}}{2\Delta x}+F_x\\
&C_{\mathrm{W}}v_{i-1,j,k}+C_{\mathrm{E}}v_{i+1,j,k}+C_{\mathrm{S}}v_{i,j-1,k}+C_{\mathrm{N}}v_{i,j+1,k}+C_{\mathrm{B}}v_{i,j,k-1}+C_{\mathrm{T}}v_{i,j,k+1}+C_{\mathrm{C}}v_{i,j,k}\\
&\quad=\frac{v^0_{i,j,k}}{\Delta t}-\frac{p_{i,j+1,k}-p_{i,j-1,k}}{2\Delta y}+F_y\\
&C_{\mathrm{W}}w_{i-1,j,k}+C_{\mathrm{E}}w_{i+1,j,k}+C_{\mathrm{S}}w_{i,j-1,k}+C_{\mathrm{N}}w_{i,j+1,k}+C_{\mathrm{B}}w_{i,j,k-1}+C_{\mathrm{T}}w_{i,j,k+1}+C_{\mathrm{C}}w_{i,j,k}\\
&\quad=\frac{w^0_{i,j,k}}{\Delta t}-\frac{p_{i,j,k+1}-p_{i,j,k-1}}{2\Delta z}+F_z
\end{aligned}\tag{8}$$

$$\begin{aligned}
&\frac{p_{i+1,j,k}-2p_{i,j,k}+p_{i-1,j,k}}{\Delta x^2}+\frac{p_{i,j+1,k}-2p_{i,j,k}+p_{i,j-1,k}}{\Delta y^2}+\frac{p_{i,j,k+1}-2p_{i,j,k}+p_{i,j,k-1}}{\Delta z^2}\\
&\quad=-\left(\frac{\xi_{i+1/2,j,k}-\xi_{i-1/2,j,k}}{\Delta x}+\frac{\eta_{i,j+1/2,k}-\eta_{i,j-1/2,k}}{\Delta y}+\frac{\zeta_{i,j,k+1/2}-\zeta_{i,j,k-1/2}}{\Delta z}\right)\\
&\qquad+\frac{D_{i,j,k}}{\Delta t}+\frac{\partial F_x}{\partial x}+\frac{\partial F_y}{\partial y}+\frac{\partial F_z}{\partial z}
\end{aligned}\tag{9}$$

where

$$C_W = -\frac{u^*}{2\Delta x} - \frac{1}{Re\Delta x^2}, \quad C_E = \frac{u^*}{2\Delta x} - \frac{1}{Re\Delta x^2}$$

$$C_S = -\frac{v^*}{2\Delta y} - \frac{1}{Re\Delta y^2}, \quad C_N = \frac{v^*}{2\Delta y} - \frac{1}{Re\Delta y^2}$$

$$C_B = -\frac{w^*}{2\Delta z} - \frac{1}{Re\Delta z^2}, \quad C_T = \frac{w^*}{2\Delta z} - \frac{1}{Re\Delta z^2}$$

$$C_C = \frac{1}{\Delta t} + \frac{2}{Re\Delta x^2} + \frac{2}{Re\Delta y^2} + \frac{2}{Re\Delta z^2}$$

$$D_{i,j,k} = \delta_x u_{i,j,k} + \delta_y v_{i,j,k} + \delta_z w_{i,j,k}$$

$$\xi_{i,j,k} = (u_{i,j,k}\delta_x + v_{i,j,k}\delta_y + w_{i,j,k}\delta_z)u_{i,j,k}$$

$$\eta_{i,j,k} = (u_{i,j,k}\delta_x + v_{i,j,k}\delta_y + w_{i,j,k}\delta_z)v_{i,j,k}$$

$$\zeta_{i,j,k} = (u_{i,j,k}\delta_x + v_{i,j,k}\delta_y + w_{i,j,k}\delta_z)w_{i,j,k}$$

Here $(\delta_x, \delta_y, \delta_z)$ represent the central second-order finite difference approximations for the first-order derivatives. It should be noted that u^*, v^*, w^* contained in the coefficients, i.e. the nonlinear terms of the momentum equations, are updated every iteration to achieve a more accurate time-dependent solution.

2.3. *Local mesh refinement*

To precisely solve the boundary layer, a local mesh refinement technique is designed in our code. The grid system suited for a local mesh refinement method is presented in Figure 4. First, the full computational domain is equally spaced with the same grid size in three directions, i.e. $\Delta x = \Delta y = \Delta z = 0.05$. Then the local mesh refinements are carried out by a

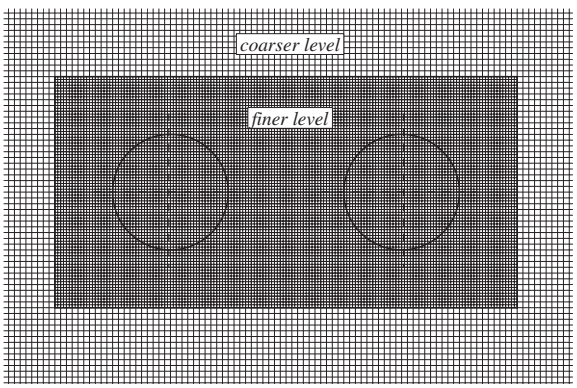

Figure 4. Local refinement grid system used in present study.

finer grid level covering a cuboid sub-region wherein the two bodies are contained. The grid size of the finer grid level is set to be 0.025. The size of the sub-domain covered by the fine grid layer is $(L+2)\times 2\times 2$, where L is the gap between the two spheres.

The full-approximation-storage (FAS) multigrid method [15] is applied to the refinement level in our code. The FAS algorithm in which the full solution is calculated at all levels is specially suited for the solution of nonlinear partial differential equations. This is different from other multigrid algorithms which calculate residuals and corrections instead of the full solution at coarser grid levels. For the present local refinement multigrid, the coarse-grid correction is performed only at the finer grid level of the sub-region containing the two bodies, while in the other sub-regions with coarser grid levels the discrete governing equations are solved directly to achieve the flow field. It should be taken into account that the interior boundaries of the refinement level are not the physical boundaries of the computational domain and no corresponding conditions can be defined. In order to couple the calculated data in different regions, the flow values at interior boundaries of the finer grid level are interpolated linearly from the coarser level.

A complete local refinement multigrid cycle marching a time step is given as follows:

(1) Obtain the values at interior boundaries of the finer level by a linear interpolation.
(2) Calculate difference equations given in Equations (8) and (9) at the finer grid level containing two bodies. For the sake of simplicity, we rewrite the difference equations as

$$\begin{aligned} L_u^h u^h &= f_u^h \\ L_v^h v^h &= f_v^h \\ L_w^h w^h &= f_w^h \\ L_p^h p^h &= f_p^h \end{aligned} \tag{10}$$

where the symbol $L_{(\cdot)}^{(\cdot)}$ denotes the nonlinear operator of the governing equations and $f_{(\cdot)}^{(\cdot)}$ is the source term. The superscript 'h' denotes the variable for finer grid level.
(3) Successively, in the sub-region containing two bodies, we achieve solution at the coarser grid level which is overlapped with the finer grid level. The equations applied here have a little difference from these in the first step. The values of physical properties needed in the source terms are interpolated from the flow field values in finer level, which is called a restriction process. The corresponding difference equations are given in Equation (11).

$$\begin{aligned} L_u^{2h} u^{2h} &= f_u^{2h} = L_u^{2h} \mathbf{I}_h^{2h} u^h + \mathbf{I}_h^{2h} (f_u^h - L_u^h u^h) \\ L_v^{2h} v^{2h} &= f_v^{2h} = L_v^{2h} \mathbf{I}_h^{2h} v^h + \mathbf{I}_h^{2h} (f_v^h - L_v^h v^h) \\ L_w^{2h} w^{2h} &= f_w^{2h} = L_w^{2h} \mathbf{I}_h^{2h} w^h + \mathbf{I}_h^{2h} (f_w^h - L_w^h w^h) \\ L_p^{2h} p^{2h} &= f_p^{2h} = L_p^{2h} \mathbf{I}_{\mathrm{h}}^{2h} p^h + \mathbf{I}_h^{2h} (f_p^h - L_p^h p^h) \end{aligned} \tag{11}$$

where $\mathbf{I}_h^{2h}$ is a operator which defines the restriction process mentioned above.

(4) A correction process (Equation (12)) is performed in the sub-region where two grid levels overlap.

$$\begin{aligned} u^h &= u^h + \mathbf{I}_{2h}^h(u^{2h} - \mathbf{I}_h^{2h}u^h) \\ v^h &= v^h + \mathbf{I}_{2h}^h(v^{2h} - \mathbf{I}_h^{2h}v^h) \\ w^h &= w^h + \mathbf{I}_{2h}^h(w^{2h} - \mathbf{I}_h^{2h}w^h) \\ p^h &= p^h + \mathbf{I}_{2h}^h(p^{2h} - \mathbf{I}_h^{2h}p^h) \end{aligned} \tag{12}$$

where $\mathbf{I}_{2h}^h$ is a prolongation operator which transferring data from coarser grids to finer grids. Here, a linear interpolation is used for the prolongation.

(5) Calculate difference equations given in Equations (8) and (9) in other sub-regions where no finer grids exist. The above computational cycle repeats until a steady or a periodic solution is achieved.

For restriction the flow values at coarser grid level are computed using a seven-points interpolation from the finer grid level, e.g.

$$\begin{aligned} u_{i,j,k}^{2h} = \tfrac{1}{12}(&6u_{2i-1,2j-1,2k-1}^h + u_{2i-2,2j-1,2k-1}^h + u_{2i,2j-1,2k-1}^h \\ &+ u_{2i-1,2j-2,2k-1}^h + u_{2i-1,2j,2k-1}^h + u_{2i-1,2j-1,2k-2}^h + u_{2i-1,2j-1,2k}^h) \end{aligned} \tag{13}$$

and similarly for values of v, w, p. The same restriction operator has been used for the residuals of Equation (11).

3. PARAMETER REQUIREMENT AND CODE VALIDATION

A cuboid domain containing two spheres placed in a tandem arrangement is solved. The width and height are $10.0D$ and the computational domain has a small blockage ratio of about 1.0%. The distance from the inlet to the centre of the left sphere is 3 diameters, 12 diameters between the centre of the right sphere and the outlet. Due to the existence of a body, the perturbation decay away from the body at a rate of $1/r^3$ (see Reference [16], where r is the distance from the centre of the body. Hence, it is appropriate that a boundary condition with a free stream velocity of $u = 1$ is applied to the inlet and the outer transverse boundaries. Because we mainly focus on the physical behaviour of the near wake, the downstream extent of the computational domain is limited to 12 diameters. Two or three wake cycles can be well computed in the downstream flow field with the present dimension. As a remedy of this shortcoming resulted from the deficient extent in the x direction, a nonreflecting condition is applied to the outflow boundary, i.e. $\partial\mathbf{u}/\partial t + u_{\text{aver}}\partial\mathbf{u}/\partial n = 0$, where u_{aver} is the averaged streamwise velocity obtained at outlet.

Extensive experiments have proved that the boundary layer on sphere does not become turbulent until a large Re of the order 10^5 is reached. Hence, the estimate of the boundary layer thickness for low Re ($\leqslant 300$) flow can be performed according to the laminar boundary layer

theory, i.e. $\delta \approx 1.10\sqrt{1/Re}$. That is to say, the present finer grid level ($\Delta x = \Delta y = \Delta z = 0.025$) containing the two bodies can well solve the boundary layer.

In order to test the time accuracy of our code, the flow past a single sphere at $Re = 275$ is computed. The calculation with a time step of 0.01 marched until a single-frequency flow is obtained and then the calculation continued with a reduced time step of 0.005 (Figure 5). The difference between the two values of St is less than 0.1% which is negligible and the time step 0.01 is chosen for all the simulations with CFL = 0.4 for the finer grid level.

To this stage, the computational parameters have been chosen appropriately and the flow of a single sphere is solved for a series of Reynolds numbers to validate the code. Figure 7 presents the wake structures at a few typical Reynolds numbers. In present study, the calculated vortical structure is visualized using the definition of a vortex as a connected region containing two negative eigenvalues of the $\mathbf{S}^2 + \mathbf{\Omega}^2$ tensor (here $\mathbf{S}$ and $\mathbf{\Omega}$ are, respectively, the symmetric and antisymmetric parts of the velocity gradient tensor) proposed by Jeong and Hussain [17] (the same below). From Figure 7 two bifurcations are well captured and the two Reynolds numbers of transitions ($200 < Re_{c1} < 225, 250 < Re_{c2} < 275$) compare well with the experimental results. The wake length is given as a function of Re in Figure 6 along with the available numerical [18] and experimental [1] data. The present wake length appears to follow an approximately logarithmic relationship with the Reynolds numbers considered here. In the first section, it was mentioned that Taneda reported the wake unsteadiness at about $Re = 130$ which has not been successfully repeated by the other simulations and experiments. This fact results in the distinct discrepancy in Figure 6. Additionally, from the extrapolated curve (denoted by dotted line), we know that the recirculation bubble does not occur until a Re of about 25.

In order to examine the unsteady force behaviour at a Reynolds number of 275, three components of the force vector acting on the sphere are defined, i.e. the drag C_D, the lateral and side force C_L and C_S. The side force is defined for the force normal to the flow symmetry plane. The lateral force is parallel to the symmetry plane. It is found that C_S is always zero. At the Reynolds number of 275, the computed average values of C_D and C_L are 0.66 and

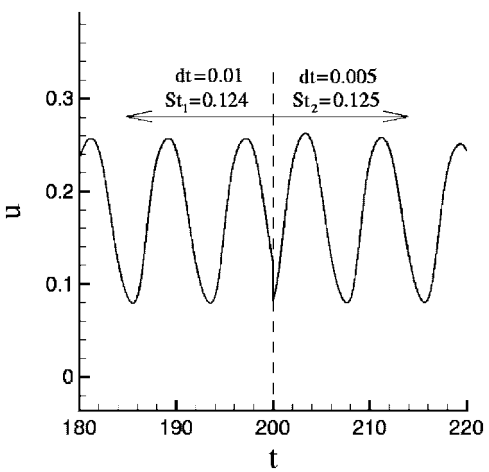

Figure 5. St number for different time increments.

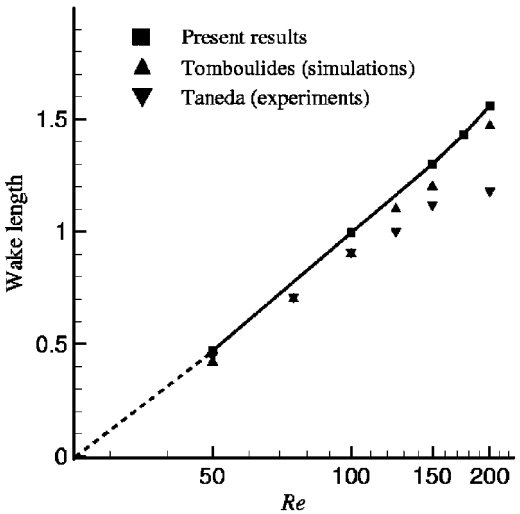

Figure 6. Wake length vs *Re*.

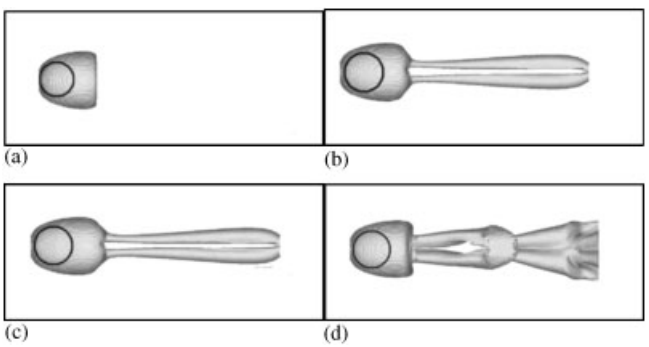

Figure 7. Wake structure for flow of a single sphere with different Reynolds numbers: (a) $Re = 200$; (b) $Re = 225$; (c) $Re = 250$; and (d) $Re = 275$.

0.061, with respective oscillation amplitudes of 0.0026 and 0.014. Johnson and Patel [4] have given the corresponding results of $C_D = 0.656$ and $C_L = 0.069$ at a Reynolds number of 300.

4. WAKE STRUCTURES AT VARIOUS SPACING RATIOS

The effect of the spacing ratio on the flow past two spheres is studied in this section. The 3D sketch of the physical model is provided in Figure 8. A few interesting regimes of interaction are observed depending on the spacing ratio L/D, where L is the distance between the centres

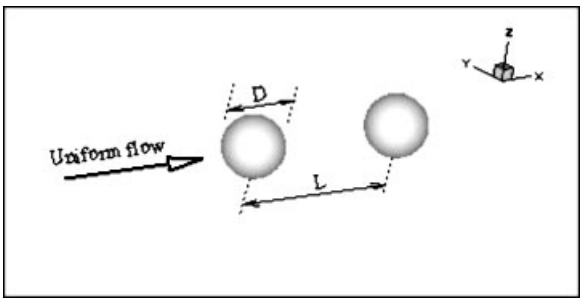

Figure 8. The 3D sketch of the physical model.

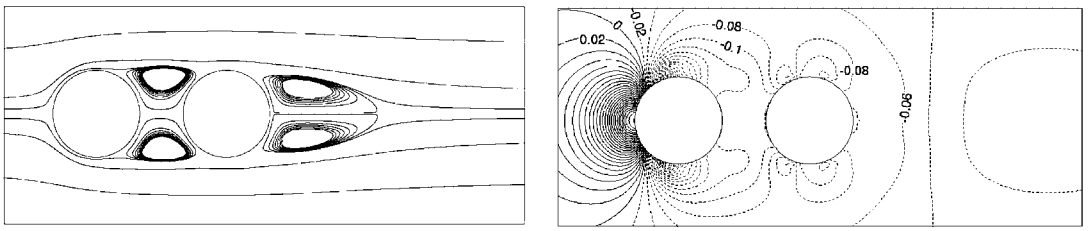

(a) (b)

Figure 9. Flow field for $L/D = 1.5$: (a) streamlines; and (b) pressure contours.

of the two spheres. The numerical results are presented in the following sub-sections. All the computations are carries out at a Reynolds number of 250.

4.1. Axisymmetric steady flow

From the experimental result for the flow of a single sphere, we know the first transition Re is about 210 over which the axisymmetric behaviour of the flow is lost. But for the case of two spheres with a small spacing ratio ($L/D = 1.5$), the computation will finally come to an axisymmetric flow at $Re = 250$. From the contours of pressure for flow of a single sphere at $Re = 250$ (see Figure 14 in Reference [4]), we know that the vortex ring in the near wake contains a global pressure minimum in the vortex centre. Therefore, if another sphere is placed within the region of the vortex ring, i.e. the case of two spheres with a small spacing ratio, the instability connected to the ring of low pressure in the wake will be eliminated and the flow has a tendency to restore the axisymmetric behaviour.

From Figure 9(a), a vortex ring with a cross plane of symmetry is embedded in the gap, no reattachment point at the central line. For this upstream vortex ring, the separation angle θ is 56.9° (note: the separation angle is measured from the rear stagnation point of each sphere), the distance between the two vortex-centres l is 0.86 and the distance between the vortex centre and the rear stagnation point d is 0.29. The corresponding values for the downstream bubble are $\theta = 48.0°$, $l = 0.62$, $d = 0.37$, respectively. Pressure coefficient contours are given

in Figure 9(b). The contours are plotted for every 0.02 increment, with the dashed lines used for the negative values. There is no pressure minimum in either the upstream wake or the downstream wake. That is to say, for the flow with small spacing ratio less that 1.5, the centrifugal force of the vortex's rotation is mainly balanced by the viscous force.

4.2. Plane-symmetric steady flow

As the spacing ratio increases to 2.0, a steady but nonaxisymmetric flow is computed after a large number of time steps. The computed flow now is characterized with a plane of symmetry.

The location of the plane of symmetry is determined only by the nonphysical factor of the numerical method applied. The flow past spheres with large enough spacing ratio is unstable. For simulations, the numerical disturbance introduced by the computation will induce the instability. But the actual position of the plane of symmetry cannot be predicted by the governing equations, in advance. From the calculations of the other CFD researchers and the authors, we knew that the position was determined by the direction of grid lines, the sweeping direction, the algorithm and the special programming code. In present computation, the plane of symmetry coincides with the plane 45° off the x–y coordinate plane.

The projected streamlines on the two planes, one 45° off the x–y coordinate plane (denoted by $Pxy1$) and the other $-45°$ off x–y coordinate plane (denoted by $Pxy2$), are drawn in Figure 10(a) and 10(b), respectively. Due to the out-of-plane velocity components, the streamlines constructed in the $Pxy2$ (Figure 10(b)) are not the real 3D streamlines. This can be

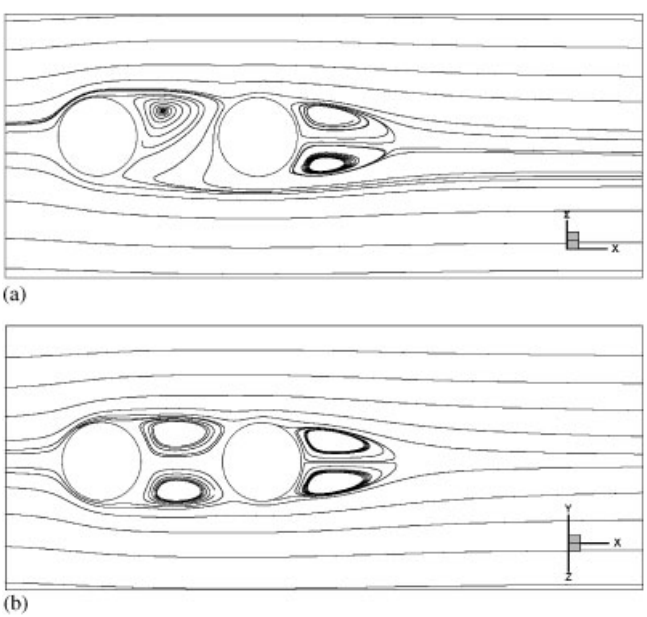

Figure 10. Streamlines for $L/D = 2.0$: (a) view on plane with an angle of 45° from x–y coordinate plane; and (b) View on plane with an angle of $-45°$ from x–y coordinate plane.

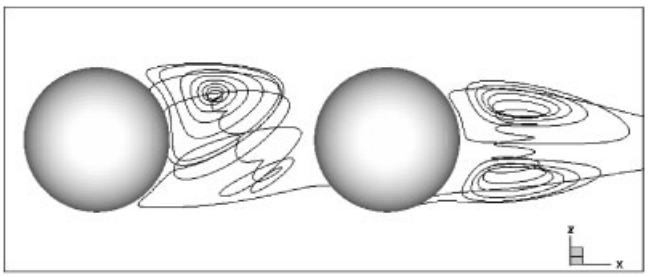

Figure 11. Particle lines for $L/D = 2.0$.

deduced from the fact that the size of the upstream vortex ring is not kept constant in the circumferential direction. Unlike the vortex rings of the case with a spacing ratio 1.5, the present vortex rings are no longer closed separation bubbles; in fact, the fluid transportation in circumferential direction is observed in Figure 11.

Figure 11 gives the paths of a pair of particles originated from the rear of left and right spheres. The circumferential motion of the fluid is clearly observed. The pathline of the particle released from the rear stagnation of the left sphere spirals clockwise into the lower focus of the near wake and then feeds into the upper focus, where it spirals clockwise outward, eventually escapes from the focus. The pathline of the particle released from the right sphere has a similar trace.

Pressure contours on the two planes, i.e. $Pxy1$ and $Pxy2$, are plotted in Figure 12 and the symmetry of the flow field is observed again. Now the pressure minimum occurs in the region of the upstream vortex ring and the value of the minimum varies slightly along the circumferential coordinate. It can be deduced that this circumferential pressure gradient induces the circumferential motion of fluid. The pressure gradient in the downstream near wake is faint compared to the upstream one, but the circumferential motion of fluid has been captured in the same way (Figure 11).

4.3. Unsteady flow

As the spacing ratio increases to $L/D = 2.5$, the periodically oscillating flow is computed. No attempt is made to further narrow the interval of the onset of the transition, due to the expensive computation.

4.3.1. Detail flow visualization at $L/D = 3.0$. The case for $L/D = 3.0$ is picked up as an example to give a detail investigation for the unsteady flow of two spheres in tandem arrangement. The shedding process of the wake in a full cycle is clearly illuminated in Figure 13. A plane of symmetry which is actually the plane $Pxy1$ mentioned previously persists through the complete unsteady shedding process. In the gap, a side-shedding pattern occurs like the case of a single sphere. At $t = 0$, a structure exists at the rear of the left sphere with its head part captured by the right sphere. At $t = \frac{1}{4}T$, a new generated structure can be seen protruding from the head part of the structure in the gap along the streamwise direction. The new structure breaks away from the parent body and develops to a full hairpin-shaped structure at $t = \frac{2}{4}T$.

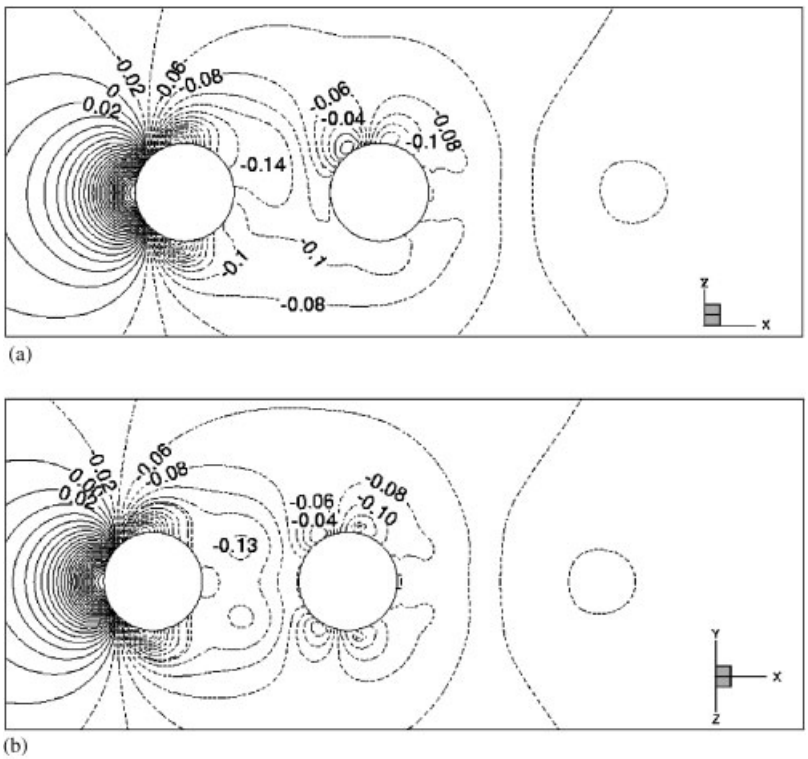

Figure 12. Contours of pressure for $L/D = 2.0$: (a) view on plane with an angle of 45° from x–y coordinate plane; (b) view on plane with an angle of −45° from x–y coordinate plane.

Then the newly formed structure begins to transfer downstream. So one of the two vortical structures existing in the far flow field originates from the head part of the structure in the gap. Another vortical structure originates from the upside of the rear of the right sphere. It is interesting that the shedding process of the latter one structure is finished in a time of about $\frac{1}{2}T$ ($\frac{3}{4}T$->$\frac{7}{8}T$->0->$\frac{1}{8}T$), i.e. a half of the shedding period of the former one structure, which is revealed by the spectra of the flow field (Figure 18) where two harmonies f_s and $2f_s$ exist ($f_s = 1/T$). While, in the other time slices of a cycle, the wake structure in the upside of the right sphere goes on with only a little change.

From the iso-surface of streamwise vorticity given in Figure 14 (the positive and negative values are denoted by white and black colours, respectively), it is known that the body of the vortical structure is composes of two vortical tubes with different rotational directions. In Figure 14, the head of the vortical structure originating from the upside of the right sphere is not identified as a vorticity region and the shedding with the harmony of $2f_s$ is not clearly observed.

To deeply understand the fluid motion, the topology of the cross flow in each of the eight sections denoted in Figure 13(a) is presented in Figure 15. The extent of the sphere's perimeter is indicated by the dashed circle. For two constant x planes in the near wake of the left sphere and right sphere, respectively, the streamlines constructed from y and z velocity

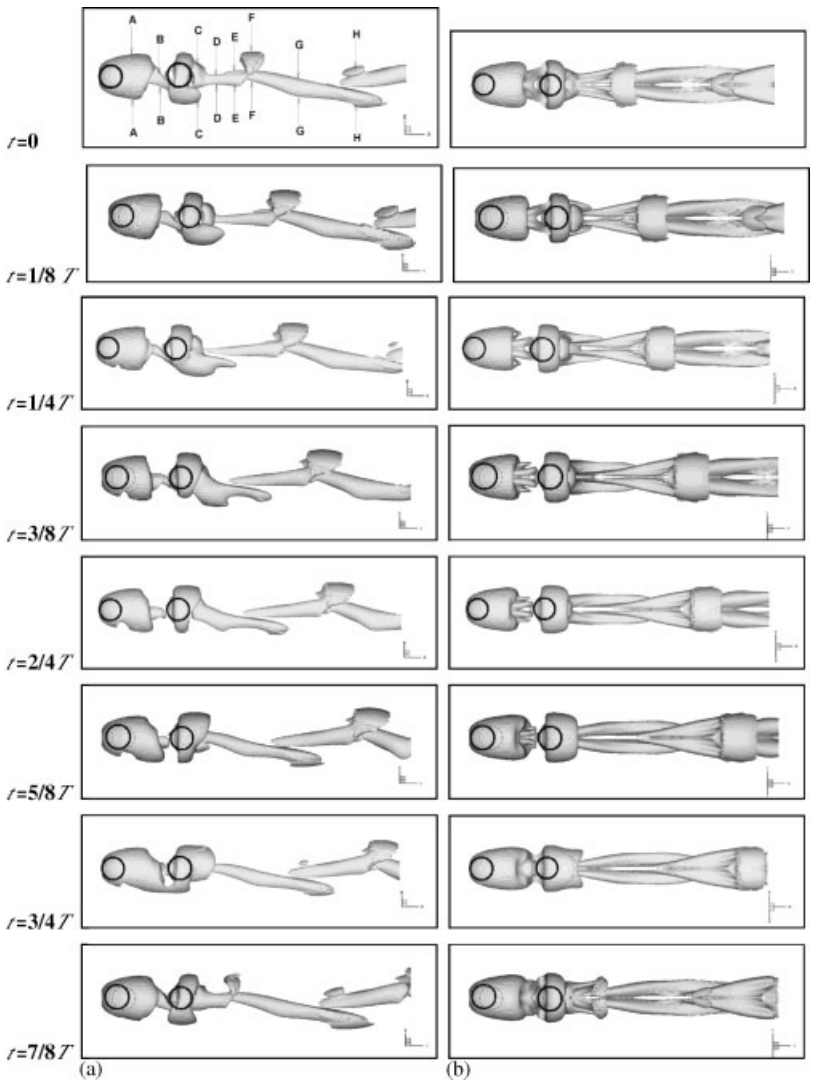

Figure 13. Wake structures in a cycle for $L/D = 3.0$: (a) $Pxy1$ plane; and (b) $Pxy2$ plane.

components are plotted in Figure 15(a) and 15(c). The contours in Figure 15(a) and 15(c) constitute two nodes, respectively, one is unstable and the other is stable. The steamlines near the projected perimeter of the sphere become curved due to the induced velocity in this region. The whirling motion of the body part of the vortical structure in the gap is evident in Figure 15(b) where two stable focuses with different spiral directions exist. The similar flow topology is seen in Figure 15(g) for the body part of the structure which is shed from the lower side of the right sphere. For the structure which originates from the upper side of the right sphere, no evident whirling motion indicated by the contours of stream-function is

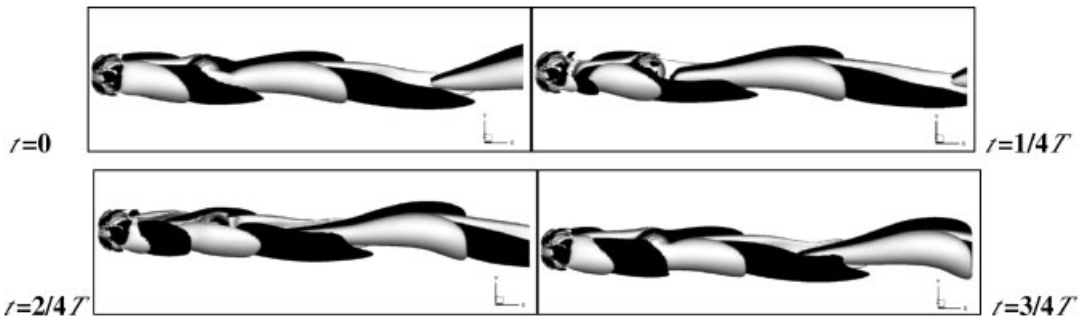

Figure 14. Oblique views of the iso-surface of ω_x in a cycle for $L/D = 3.0$.

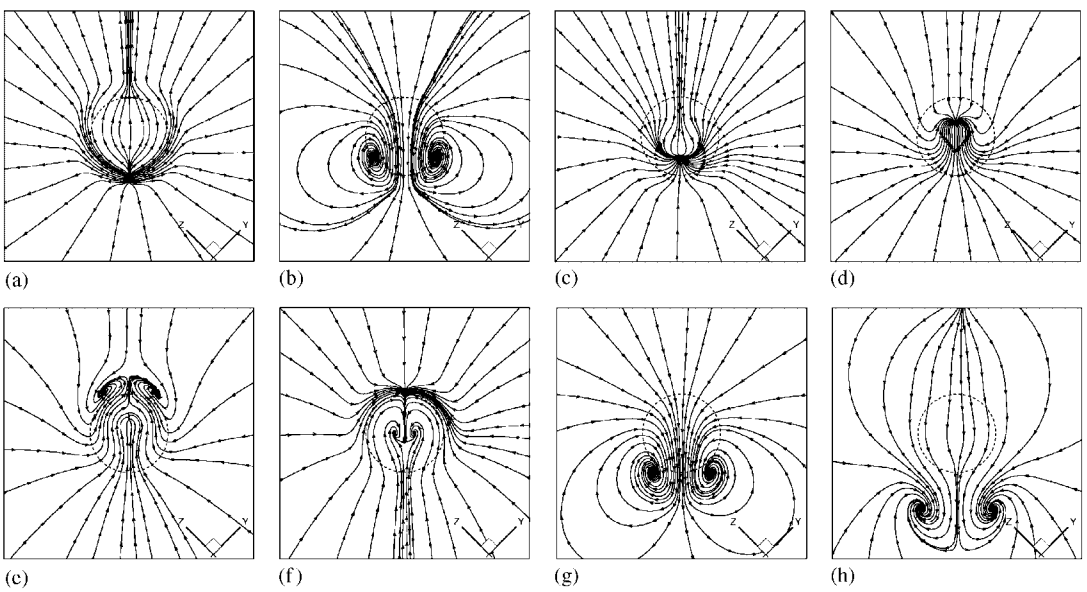

Figure 15. Flow topology on eight typical cross sections for $L/D = 3.0$: (a) section-A; (b) section-B; (c) section-C; (d) section-D; (e) section-E; (f) section-F; (g) section-G; and (h) section-H.

observed on the cross section of the body part; but it is identified as a vortical region by Jeong and Hussain's method. Figure 15(e) and 15(f) provide information on the flow behaviour in the region of the tail of the wake structure shed from the lower side of the right sphere and the head of the structure from the upper side. The tail of the structure from the lower side is characterized by a pair of closed stable focuses connected with a saddle point. But the head of the structure from the upper side does not contain any focus yet. The cross flow further downstream is presented in Figure 15(h) and the focuses corresponding to the structure from

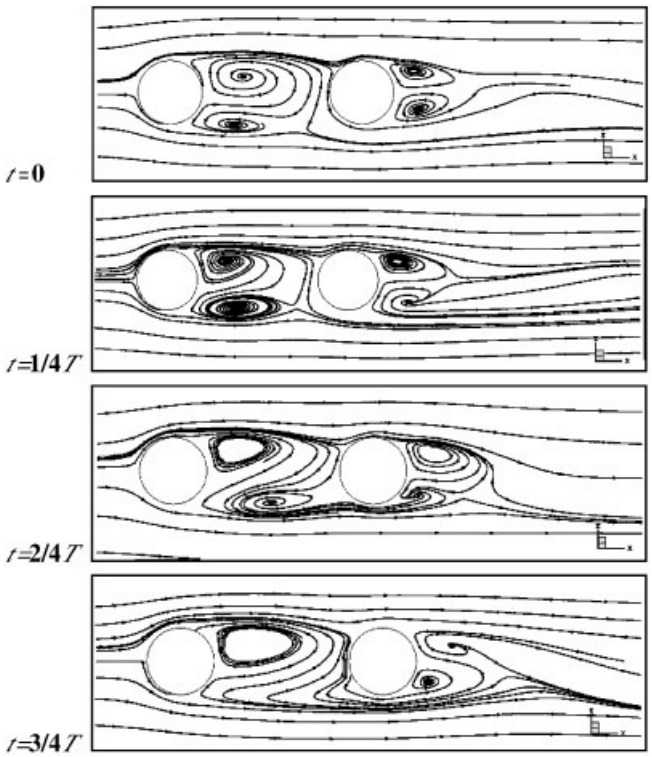

Figure 16. Instantaneous streamlines in a cycle for $L/D = 3.0$.

the lower side are observed to move down to the lower part of Figure 15(h) compared with their positions in Figure 15(g).

To further investigate the flow behaviour, the instantaneous streamlines in the plane of symmetry (the plane denoted by $Pxy1$) are given sequentially in a period (Figure 16) and the instability behaviour of the flow topology during the shedding process can be clearly obtained. In the upper side of the gap, an unstable focus captures both the two spheres and the unstable behaviour holds in the full period. In the lower side of the left sphere, a stable focus appears at the beginning of a period. At $t = \frac{1}{4}T$, this focus evolves into a limit cycle onto which streamlines converge from both sides. The appearance of the limit cycle indicates the shift of the focus from stable to unstable. At the next quarter, there is an unstable focus on the lower side of the left sphere and the limit cycle is not present anymore. For the wake of the right sphere, the two rings are stable and unstable, respectively, in the first half period. In the second half period, an unstable focus is present in the upper side and a stable one in the lower side, instead.

The topology of the limiting streamlines over the rear of the two spheres is plotted in Figure 17. The limiting flow behaviour of the left sphere is similar to that of the case of a single sphere. That is to say, the separation line of the left sphere remains essentially stationary along the full period and the change of the position of the stagnation point is hardly noticed.

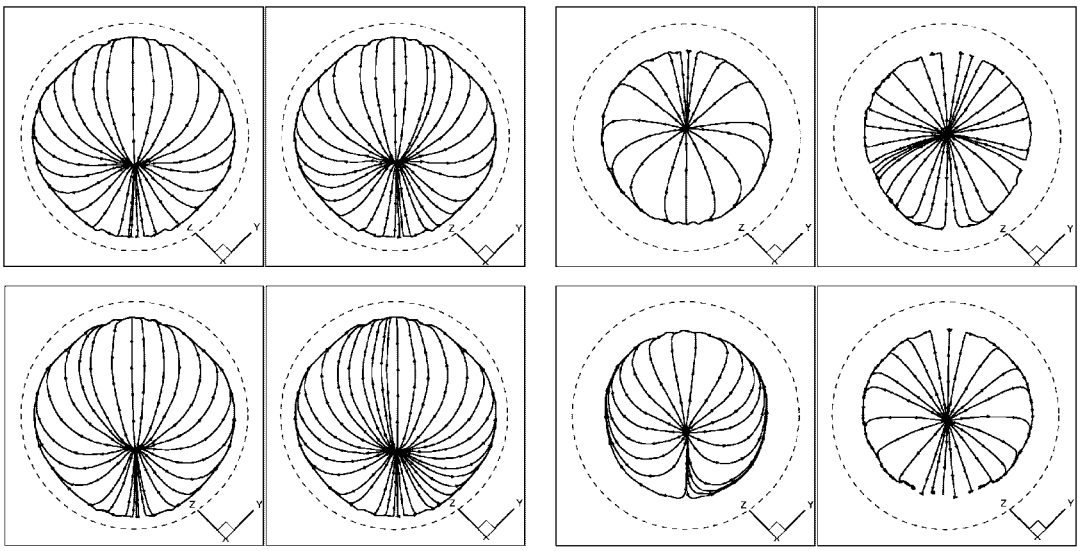

Figure 17. Rear surface-limiting streamlines in a cycle for $L/D = 3.0$: (a) every quarter period for left sphere; and (b) every quarter period for right sphere.

But it is not the case for the right sphere. The position of the saddle point on the separation line of the rear of the right sphere changes alternatively in a period, in top side for the first half period and in bottom side for the second half period.

4.3.2. Dynamic behaviour for various spacing ratios. In our computation, two monitors are arranged along the x-axis in the upstream wake and the downstream wake: one is placed in the midplane of the gap and the other in the plane with two diameters from the second sphere. The flow spectra of the wake are determined from the streamwise velocity fluctuation of the monitor point by an FFT technique. Figure 18 provides the spectra for the spacing ratios ranging from 2.5 to 4.5. At $L/D = 2.5$, a faint wavy flow is detected in the wake. The weakly oscillating upstream wake has a shedding frequency of $f_s = 0.12$. The shedding frequency $f_s = 0.12$ can also be detected in the spectra of the downstream wake. Furthermore, a $2f_s$ harmony is noticeable in the downstream spectra, though its amplitude is smaller than the dominated frequency f_s. From previous study, it is known that the f_s frequency component in the downstream spectra corresponds to the vortex shedding from the lower side of the right sphere, the $2f_s$ harmony corresponding to the shedding from the upper side of the right sphere. The spectra contains of the upstream wake have little difference between various spacing ratios. But the $2f_s$ harmony in the downstream spectra is enhanced with the increase of the spacing ratio. With a small increment of 0.5 from $L/D = 3.0$ to $L/D = 3.5$, the $2f_s$ harmony begins to play the dominated role in the spectra. Hence, a critical spacing ratio $(L/D)_{cr}$ is thought to exist in the interval between 3.0 and 3.5. In the two sides of the critical spacing ratio, the two structures with different shedding frequencies have different intensity.

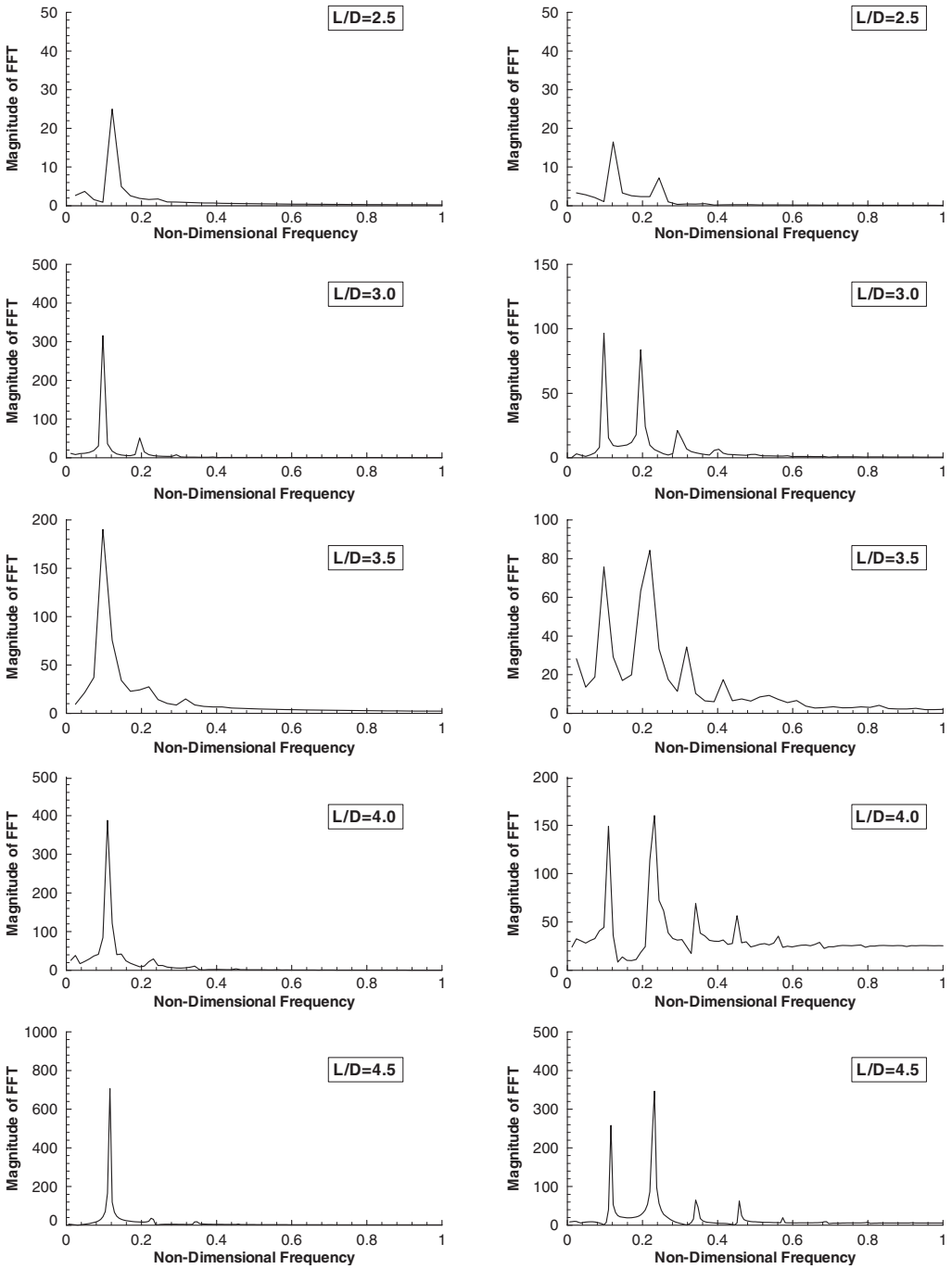

Figure 18. Flow spectra in wakes (left column corresponds to the upstream wake and right column for the downstream wake).

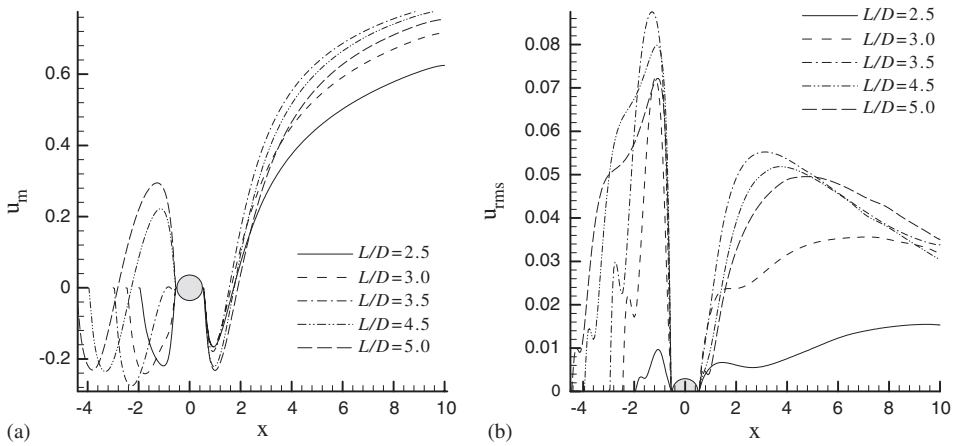

Figure 19. (a) Mean streamwise velocity along the axis; and (b) RMS streamwise velocity along the axis.

The streamwise velocity along the central line of the domain for the average flow is plotted in Figure 19(a) and the same plot for the streamwise RMS velocity in Figure 19(b). The hatched circle zone denotes the position of the right sphere. The values of the average velocity on the central line in the gap are found to be negative for spacing ratio $L/D \leqslant 3.0$. As the spacing ratio increases to 3.5, a small region with positive average velocity appears abruptly in the gap, which indicates that the recirculation region is no longer captured by the right sphere. At larger spacing ratio ($L/D = 4.5$ or 5.0), the average velocity is positive in a broader region near the right sphere. For $L/D = 5.0$, the two regions with negative and positive velocity are symmetric about the midplane of the gap. While for the near wake of the right sphere, there is little difference between the curves of average velocity at various spacing ratios. The end of the recirculation region along the axis is at 1.227 diameters downstream from the rear of the right sphere. The experimental value of the extent of the recirculation region is 1.337 for the flow past a single sphere at $Re = 280$ provided by Wu and Faeth [19].

In Figure 19(b), it is revealed that the maximum RMS value in the central line is less than 10% of the freestream velocity. From the RMS plot, we can judge that there is a violent wake region which is very close to the front of the right sphere in the gap. For each spacing ratio, there are two local maximum RMS values in the gap and in the downstream wake, respectively. The two maximum values grow slowly as the spacing increases and come to the peak values at about $L/D = 3.0$ which is the critical spacing ratio mentioned previously.

Figure 20 gives the streamlines in the plane of symmetry at $L/D = 3.5$. It is clear that in current spacing ratio, the vortex ring in the gap is no longer captured by the right sphere and the transverse motion of fluid across the gap becomes evident. More upstream streamlines pass through the gap, directly flow around the right sphere, and eventually join into the downstream flow. The flow given in Figure 20 is consistent with the average velocity curves in Figure 19(a) where the region with positive velocity begins to occur in the gap at about $L/D = 3.5$.

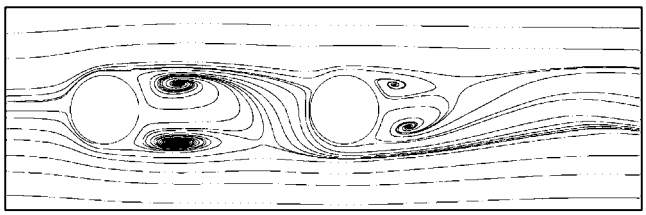

Figure 20. Streamlines for $L/D = 3.5$.

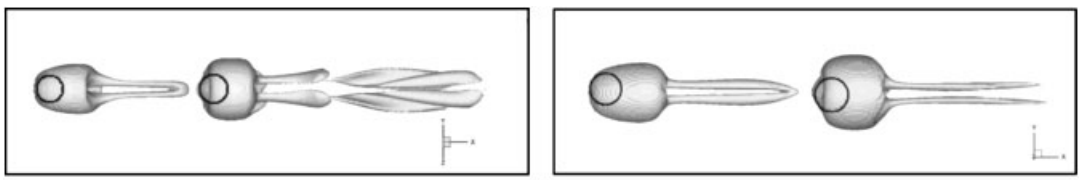

Figure 21. Wake structure for large gaps: (a) view in $Pxy1$ plane for $L/D = 6.0$; and (b) view in (x, y) plane for $L/D = 7.0$.

For spacing ratio larger than 6 diameters, only a very weak coupling is observed, leading to the disappearance of the hairpin-shaped vortex in the gap (see Figure 21(a)). At $L/D = 7.0$, the whole flow field is characterized by two stable double-threads vortical structures in the gap and in the downstream wake (see Figure 21(b)). This indicates that the two spheres with a gap larger than seven diameters act as a single sphere, respectively. Comparing the two plots in Figure 21, we notice that as the flow returns to be stable, the position of the symmetrical plane has a change of an angle of 45°.

5. CONCLUSION

In this paper, the virtual boundary method provided by Goldstein has been extended to a 3D application and combined with a local mesh refinement method and the computational performance has come to a distinct improvement. Then the flow field of two spheres in tandem arrangement for a series of gaps is investigated for $Re = 250$.

Due to complicated coupling between two spheres, a few interesting flow regimes are revealed, i.e. the axisymmetric flow at $L/D = 1.5$, the steady flow with a plane of symmetry at $L/D = 2.0$ and the periodic flow for $L/D > 2.5$. The present categories show a reasonable agreement with Yutaka's experimental study for the flow of two spheres at $Re = 220$. In Yutaka's results, an asymmetric flow is obtained at $L/D = 1.65$ and an intermittent vortex shedding starts at a spacing ratio of about 2.56. In our numerical study, because of the expensive computational cost, the transitional spacing ratio has not been achieved in a narrower interval.

The disharmonic shedding phenomenon is clearly revealed in the flow spectra and a critical spacing ratio is found between 3.0 and 3.5. When the spacing ratio is beyond the critical value, the streamlines become smoother near the lower side of the right sphere, which leads to the vortex structure from the upper side of the right sphere has more powerful intensity than the one from the lower side. But no distant frequency hopping occurs due to the critical spacing ratio, so this critical value is actually a 'regular spacing ratio'. This is not the case for the critical spacing ratio of the flow of two cylinders. As the gap between the two cylinders increases to the critical value, the left cylinder begins to shed vortices suddenly and the shedding frequency of the downstream cylinder presents an abrupt change.

As the spacing ratio increases from 6 diameters to 7 diameters, the direction of the symmetrical plane has a change of an angle of 45°. This interesting phenomenon of the 'jump' remains to be a question. The author suppose that it should imply a certain transition between the two diameters, because numerical conditions for all simulations with various gaps remain the same and no unphysical factors will be introduced into the computation. The author will do more work for this question in the future.

It should be noted, the virtual boundary method cannot precisely define the physical boundary or surface, i.e. the boundary in this method has a thickness of about $0.025D$ (the increment of the finer grid level) in effect.

ACKNOWLEDGEMENTS

The authors would like to express their sincere thanks to the Center for Engineering and Scientific Computation of Zhejiang University for providing the SGI Origin3900 machine for all the computational tasks. This work is a part of the VIV (Vortex Induced Vibration) research project which is supported by the National Natural Science Foundation of China (Grant No: 10272094).

REFERENCES

1. Tandea S. Experimental investigation of the wake behind a sphere at low Reynolds numbers. *Journal of the Physical Society of Japan* 1956; **11**(10):1104–1108.
2. Magvery YRH, Bishop RL. Transition ranges for three-dimensional wakes. *Canadian Journal of Physics* 1961; **39**:1418–1422.
3. Sakamoto H, Haniu H. The formation mechanism and shedding frequency of vortices from a sphere in uniform shear flow. *Journal of Fluid Mechanics* 1995; **287**:151–171.
4. Johnson TA, Patel VC. Flow past a sphere up to a Reynolds number of 300. *Journal of Fluid Mechanics* 1999; **378**:19–70.
5. Sungsu LA. Numerical study of the unsteady wake behind a sphere in a uniform flow at moderate Reynolds numbers. *Computers & Fluids* 2000; **29**:639–667.
6. Tsuji Y, Morikawa Y, Terashima K. Fluid-dynamic interaction between two spheres. *International Journal of Multiphase Flow* 1982; **8**(1):71–82.
7. Schouveiler L, Brydon A, Leweke T, Thompson MC. Interactions of the wakes of two spheres placed side by side. *European Journal of Mechanics B/Fluids* 2004; **23**:137–145.
8. Kim I, Elghobashi S. Three-dimensional flow over two spheres placed side by side. *Journal of Fluid Mechanics* 1993; **246**:465–488.
9. Goldstein D, Handler R, Sirovich L. Modeling a no-slip flow boundary with an external force field. *Journal of Computational Physics* 1993; **105**:354–366.
10. Fadlun EA, Verzicco R, Orlandi P, Yusof M. Combined immersed-boundary finite-difference methods for three-dimensional complex flow simulations. *Journal of Computational Physics* 2000; **161**:35–60.
11. Saiki EM, Biringen S. Numerical simulation of a cylinder in uniform flow: application of a virtual boundary method. *Journal of Computational Physics* 1996; **123**:450–465.
12. Harlow FH, Welch JE. Numerical calculation of time-dependent viscous incompressible flow of fluid with free surface. *Physics of Fluids* 1965; **8**(12):2182–2189.

13. Abdallah S. Numerical solutions for the pressure Poisson equation with Neumann boundary conditions using a non-staggered grid, I. *Journal of Computational Physics* 1987; **79**:182–192.
14. Abdallah S. Numerical solutions for incompressible Navier–Stokes equations in primitive variables using a non-staggered grid, II. *Journal of Computational Physics* 1987; **70**:193–202.
15. Liu CQ. *Introduction to Multigrid Method and the Application in Fluid Dynamics.* TsingHua University Press: 1995.
16. Batchelor GK. *An Introduction to Fluid Dynamics*. Cambridge University Press: Cambridge, 1967.
17. Jeong J, Hussain F. On the identification of a vortex. *Journal of Fluid Mechanics* 1995; **285**:69–94.
18. Tomboulides AG, Orszag SA. Numerical investigation of transitional and weak turbulent flow past a sphere. *Journal of Fluid Mechanics* 2000; **416**:45–73.
19. Wu JS, Faeth GM. Sphere wakes in still surroundings at intermediate Reynolds numbers[J]. *AIAA Journal* 1993; **31**:1448.

